Computers & Graphics 102 (2022) 154–163

Contents lists available at ScienceDirect

Computers & Graphics

journal homepage: www.elsevier.com/locate/cag

Special Section on CEIG 2021

An efficient method for acquisition of spectral BRDFs in real-world scenarios

Juan M. Jurado [a,*], J. Roberto Jiménez-Pérez [a], Luís Pádua [b], Francisco R. Feito [a], Joaquim J. Sousa [b]

[a] Computer Graphics and Geomatics Group, University of Jaén, Jaén, Spain
[b] Engineering Department, University of Trás-os-Montes e Alto Douro, Vila Real, Portugal

ARTICLE INFO

Article history:
Received 14 July 2021
Received in revised form 25 August 2021
Accepted 31 August 2021
Available online 3 September 2021

Keywords:
Material appearance
Reflectance data measurements
Hyperspectral imaging
BRDF
UAV-based sensors
3D models

ABSTRACT

Modelling of material appearance from reflectance measurements has become increasingly prevalent due to the development of novel methodologies in Computer Graphics. In the last few years, some advances have been made in measuring the light-material interactions, by employing goniometers/reflectometers under specific laboratory's constraints. A wide range of applications benefit from data-driven appearance modelling techniques and material databases to create photorealistic scenarios and physically based simulations. However, important limitations arise from the current material scanning process, mostly related to the high diversity of existing materials in the real-world, the tedious process for material scanning and the spectral characterisation behaviour. Consequently, new approaches are required both for the automatic material acquisition process and for the generation of measured material databases. In this study, a novel approach for material appearance acquisition using hyperspectral data is proposed. A dense 3D point cloud filled with spectral data was generated from the images obtained by an unmanned aerial vehicle (UAV) equipped with an RGB camera and a hyperspectral sensor. The observed hyperspectral signatures were used to recognise natural and artificial materials in the 3D point cloud according to spectral similarity. Then, a parametrisation of Bidirectional Reflectance Distribution Function (BRDF) was carried out by sampling the BRDF space for each material. Consequently, each material is characterised by multiple samples with different incoming and outgoing angles. Finally, an analysis of BRDF sample completeness is performed considering four sunlight positions and 16x16 resolution for each material. The results demonstrated the capability of the used technology and the effectiveness of our method to be used in applications such as spectral rendering and real-word material acquisition and classification.

1. Introduction

Realistic appearance modelling of real-world materials has been a widely studied topic in Computer Graphics. In this context, the Bidirectional Reflectance Distribution Function (BRDF) is used to characterise the interaction of light and matter [1]. Significant advances have been proposed for modelling the material appearance from measured reflectance data so that several databases of real-world materials have been created. For instance, the Mitsubishi Electric Research Laboratories (MERL) database [2], which covers a wide variety of isotropic materials, and UTIA [3] for anisotropic materials have served as validation for many researches over the last few years [4–7].

Despite recent advances for efficient material acquisition, the generation of BRDF datasets still remains a time-consuming and tedious process, as measuring involves a four-dimensional domain at high resolution. Capturing the material appearance in different contexts has been an active research domain recently. According to the ubiquitous nature of photorealistic image generation, and emerging fields such as computational materials, the efficient acquisition of measured BRDFs, with reflectance data captured from real-world materials is valuable for many applications [1].

The use of unmanned aerial vehicles (UAVs) and hyperspectral sensors enable the capability of capturing reflected light of visible objects from the camera viewpoint. This technology is able to measure the reflectance in real-world scenarios with a high radiometric accuracy from visible and near-infrared parts of the electromagnetic spectrum (400 to 1000 nm) [8]. These sensors are mounted on UAVs to capture many hyperspectral data cubes with a high spatial resolution, depending on the flight height. Some previous methods were proposed for material-based object tracking in videos [9], material pattern matching in hyperspectral

* Corresponding author.
E-mail address: jjurado@ujaen.es (J.M. Jurado).

https://doi.org/10.1016/j.cag.2021.08.021

data [10] and detection of spectrally varying BRDF materials in hyperspectral reflectance maps [11]. Exploration of hyperspectral imaging offers a host of novel applications and researches involving material appearance modelling. In fact, some recent approaches were focused on the material characterisation by BRDFs using a goniophotometer [12]. To our knowledge, there are not previous researches that propose an efficient measurement of reflectance data in real-world scenarios using UAV-based hyperspectral sensors since most of them are based on measuring the material-light interaction in the laboratory considering specific constraints.

In this study, an innovative method for an efficient acquisition of spectral BRDF materials from the real world is presented. Along the UAV trajectory the material reflections towards different directions depending on the surface orientation are measured. After the acquisition stage, hyperspectral images are processed to correct geometric distortions and then, a semantic segmentation is performed to detect those pixels (samples) that present a similar spectral behaviour. The spectral signature is studied from 440 to 900 nanometres (nm) divided into 200 bands. Those samples which present a similar reflectance plot in the studied wavelengths are clustered to represent a total of seven materials. After the segmentation process, every sample is characterised considering the 3D geometry of the scene, the sunlight position and the viewpoint of the hyperspectral camera. Then, all samples are normalised to the BRDF coordinate system. Finally, an analysis of the BRDF occupation and distribution of samples is carried out. Our proposed method involves a disruptive solution for the acquisition of spectral BRDF materials. This research aims to enhance the BRDF measurement of real-world materials and the creation of large material databases considering the visible and non-visible range.

The paper is organised as follows: Section 2 presents the previous work. Section 3 describes the studied area, the two aerial platforms used for data acquisition, and the processing of input data. Section 4 is focused on the material segmentation. Section 5 describes, step-by-step, the characterisation of material samples. Sections 6 and 7 present and discuss the results. Finally, conclusions and future research directions are addressed in Section 8.

2. Related work

Material Acquisition. In the last few years, the availability of databases which include real-world material measurements has fuelled a considerable innovation in the development of realistic modelling of BRDF for physically based rendering (PBR). The study of material appearance has been used in Computer Graphics for multiple purposes such as photorealistic rendering [13], material perception [7] and physics-based simulations [14]. The observation of material behaviour in the real-world under variant incident illumination is a challenging task. Scattering by surfaces is the most important type of interaction typically encoded in the BRDF. The BRDF specifies the directional profile of light scattered by a surface considering an incident illumination with a specific direction. Unfortunately, the acquisition of rich sets of BRDF measurements is challenging for several reasons: (1) high dimensionality, (2) arbitrary frequency and (3) physical constraints. Several BRDF measurement techniques have been used in the acquisition process [15]. The most common types are based on goniophotometers or image-based devices. The first one uses motorised axes to illuminate and observe the sample from arbitrary directions [16]. These devices achieve an accurate measurement of material-light interactions but the acquisition is quite long if dense 4D measurements are desired [17–19]. Despite the acquisition being more efficient than the previous approach, such devices have more stringent limitations on their precision on the observable angle and some geometric constraints and it implies a high difficulty for the measurement of anisotropic samples.

Many research studies focus on analysing different properties of a given material such as viscosity, translucency, glossiness as well as particular applications like filtering [20], material editing [6,21], material synthesis [22] and BRDF compression [23]. Most of the previous studies focus on the scalar or RGB intensity of scattered light, neglecting physical features of light as its spectrum and polarisation state. In a recent study of Baek et al. [24] a comprehensive database of multispectral polarimetric reflectance of real-world objects with a data-driven polarimetric BRDF implementation was proposed. Undoubtedly, the characterisation of the material reflectance in a wide range of the spectrum (visible and non-visible) is a key property to accurately establish its appearance under complex illumination environments. Even predictive rendering requires a particularly high level of accuracy using spectral data for the material perception [25]. Nevertheless, the acquisition of BRDF samples using traditional systems (eg. goniophotometers) leads to times of approximately 2.5 h for isotropic samples and 2–3 days for anisotropic samples [12]. For this reason, there are not many spectral BRDF measurements and consequently, a limitation exists for the calculation of material appearance out of the RGB range of the spectrum.

Hyperspectral imaging. The proliferation of UAV-based sensors for the efficient acquisition of large image datasets of urban or natural scenarios enables the generation of many 3D models, applying photogrammetric techniques, and the measurement of reflected light for each object in different parts of the electromagnetic spectrum using hyperspectral sensors. Although the high level of maturity reached by UAV-based technology in terms of sensing capabilities [26], the use of hyperspectral imaging systems is still challenging. In particular, in order to fully exploit the advantages given by hyperspectral imagery it is crucial to ensure the positional accuracy. Indeed, the great radiometric diversity provided by hyperspectral sensing systems will only be useful if it is geometrically accurate, allowing quantitative analysis to be performed. A review on the published studies based on the use of UAV-based pushbroom hyperspectral systems concluded that, although widely used, the geometric rectification is still challenging [27].

In terms of the contribution of UAV-based hyperspectral imaging (HSI) for material recognition, some methods have been proposed to classify agricultural materials [28,29] and different types of human objects [30,31]. Despite its radiometric accuracy, the resulting hyperspectral images present a high geometric deformation, so that makes difficult its combination with other data sources. This problem was approached by Author1 et al. [32] and proposed a method for geometric alignment between hyperspectral images and high-resolution RGB imagery. It opens possibilities to use hyperspectral data with 3D data. To our knowledge, UAV-based hyperspectral technology has not been used in material appearance and in this work, we demonstrate their capabilities to get measured reflectance values of real-world materials and to model their appearance by the BRDF estimation.

Material databases. Regarding existing datasets with measured materials, MERL [2] is one of the most popular databases, which contains 100 BRDFs for isotropic materials. Serrano et al. 1u [6] proposed a novel methodology to extend the original MERL database to include 400 mathematical valid BRDFs. UTIA databases [3] provides a wide range of anisotropic materials with a sufficient resolution to be used for material rendering. Another previous study estimates the reflectance and natural illumination of different objects, which includes calibrated HDR information [33]. Previous material datasets require an awkward

Fig. 1. Overview of the study area.

heuristic conversion from RGB to spectra to be useable in spectral rendering. Recently, an on-going database by Dupuy and Jakob [12], which measures spectral reflectance has been provided. This contains the most fully spectral BRDFs of isotropic and anisotropic materials from the real world. The measured spectral range is from 360 to 1000 nm changing both the incident light position and the camera viewpoint. This measurement is performed using a goniometer/reflectometer which is deployed under specific laboratory conditions. This complex infrastructure involves tedious and slow processes under specific lighting conditions to measure the material appearance, especially for anisotropic features.

To overcome the mentioned limitations, we aim to use the capability of UAV-based hyperspectral sensors to propose a new way to acquire measured spectral BRDF of real-world materials. Our approach enables the characterisation of hyperspectral samples and the study of BRDF occupation according to a drone flight. Both, hyperspectral and the geometry of the study area (a 3D point cloud) are merged to characterise every material sample with the normal vector. Thus, a set of materials are studied considering the distribution of measurements and the reflectance values for each spectral band in the BRDF space.

3. UAV-based data acquisition and processing

3.1. Study area

The campus of University of Trás-os-Montes and Alto Douro was used in this study for data acquisition, as shown in Fig. 1.

The surveyed region is characterised by both natural and artificial materials. In this area some buildings, vegetation, human-made objects, gardens and roads provide us with a rich environment to measure the reflectance of different materials in a real-world scenario. This area is representative of the majority of hyperspectral use cases scenarios, as it is formed by a diversity of environments. The southernmost sector of the study area is composed of dense vegetation and the northern sector is mainly occupied by man-made linear features. In the remaining sectors there is a mixture of undergrowth and linear entities, such as roads and parking lots. Regarding the topography, the study area is characterised by a medium altitude (500 m in average).

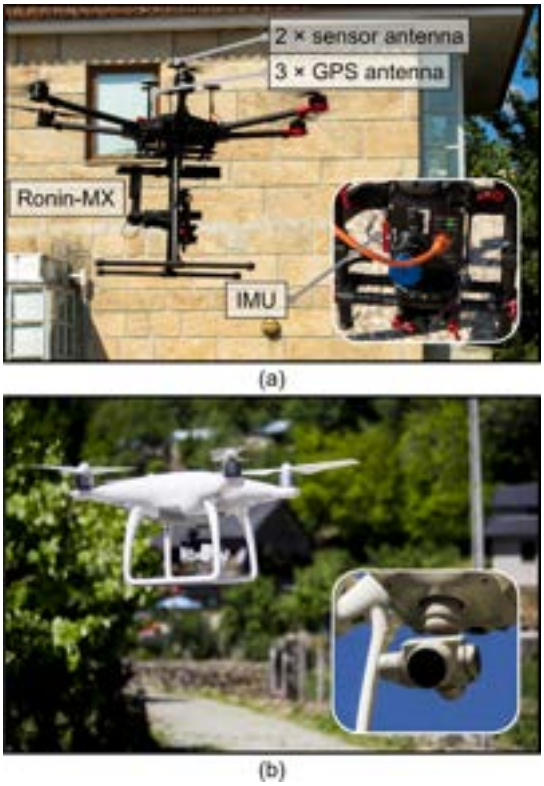

Fig. 2. Unmanned aerial vehicles and sensors used in this study, (a) the Matrice 600 Pro and the Headwall Nano-Hyperspec sensor; and (b) the DJI phantom 4, whose sensor collects RGB imagery.

3.2. Data collection

Data acquisition was carried out using two different UAVs, both produced by DJI manufacturer (Shenzhen, China), the Phantom 4 (P4) and the Matrice 600 Pro (M600). P4 is a cost-effective drone equipped out-of-the-box with a FC330 RGB camera (1/2.3" CMOS, with 12.4 megapixels). M600 was used for hyperspectral data acquisition. The used hyperspectral sensor is the NanoHyperspec VNIR (Headwall Photonics, Inc., MA, USA), mounted in the DJI Ronin-MX gimbal [26]. Fig. 2 shows the equipment used to collect both RGB images and hyperspectral data.

The Nano-Hyperspec sensor has been specifically designed for UAV-based remote sensing. The sensor, which is based on CMOS (Complementary Metal Oxide Semiconductor) technology and is lightweight at 0.52 kg. uses a 12 mm lens. The Nano-Hyperspec is a push-broom sensor, i.e., imagery is collected along the direction of flight, line by line, with each line captured at a unique moment in time, corresponding to an instantaneous position and altitude of the UAV. This means that the acquisition process captures one spectral image line at a time, which is perpendicular to the flight's direction. Each line of pixels comprises 640 spatial pixels and 270 spectral bands. In this study, only 200 spectral bands were studied since the border bands are discarded due to a high noise by the capture. Both flights were performed at the same day and time at solar noon. The sky was clear which assured uniform light conditions. The flight time was around 20 min. To ensure an adequate balance between the spatial resolution, image quality and precise data, the selected flight height was around 100 m. Despite the fact that a lower height can provide us a higher resolution of RGB and hyperspectral data, a higher geometric deformation will be presented in hyperspectral images, as concluded by Jurado et al. [32].

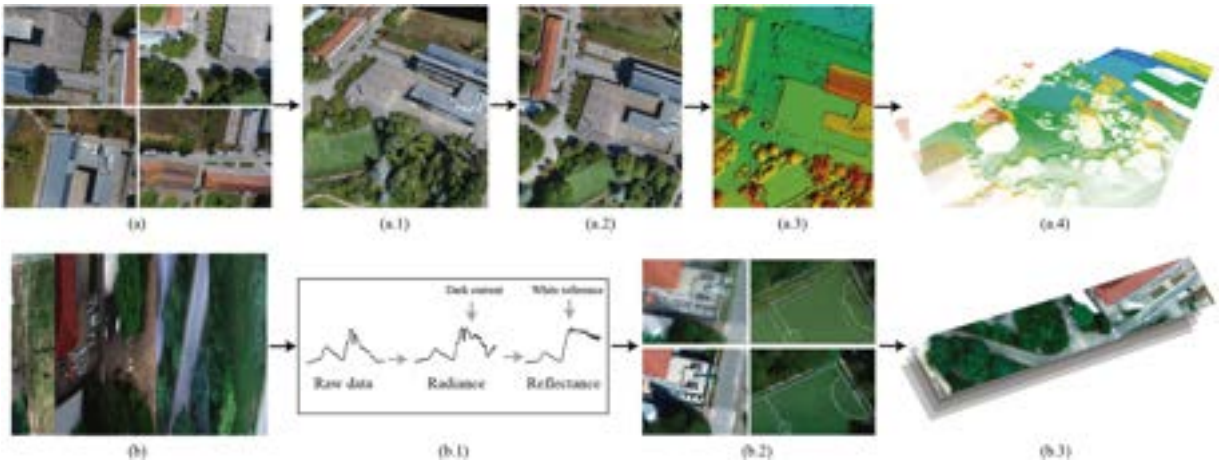

Fig. 3. Overview of data preprocessing. (a) RGB images, and (b) hyperspectral images are collected. (a.1) The dense point cloud, (a.2) the RGB orthomosaic, and (a.3) the DSM. (a.4) A resampled height map is obtained (10 cm per pixel). (b.1) Hyperspectral data are calibrated and the reflectance is estimated per pixel, (b.2) the image distortion is corrected by applying an alignment method [32]. (b.3) Orthorectified hyperspectral swaths.

On the one hand, RGB data have a spatial resolution of 6.7 cm from the take-off position, with 80% front imagery overlap and 70% side overlap between flight lines and covering approximately 5 ha. A double flight configuration and a camera angle of 70° were selected to include imagery from different perspectives in order to increase the three-dimensional information of the surveyed area [34].

On the other hand, forward motion provided by the UAV during the acquisition process, enables to scan the spectrometer's slit in a way that at each point in time – secured by the sensor's frame rate – a new line from the monitored object is acquired, as determined by the spectrometer's field-of-view (FoV). As most digital sensors, the hyperspectral sensor collects raw digital number (DN) data. DN counts are then converted into radiance, using Headwall's SpectralView software. However, in order to be able to apply that transformation, before each flight the sensor must be calibrated. This can be achieved by placing a white reference object directly in front of the lens. Full illumination happens by adjusting the white target's reflective angle relative to the sun's location, to maximise the intensity spectrum for the sensor. Lens cap is used to calibrate the sensor's dark reference. Radiance provides measurements in physical units of milliwatts per square centimetre per steradian per micrometre (mW cm^{-2} sr^{-1} μm^{-1}), thus eliminating the problem of specific measuring scales for each sensor. However, obtaining imagery in reflectance units is required for comparison purposes. In addition, for the calibration process, a calibration target with nominal reflectance values of 12%, 25%, 50%, and 90% is deployed in the terrain. Finally, as for flight encompassing hyperspectral data acquisition was performed at 100 m above ground level (spatial resolution of approximately 8 cm), maintaining a constant distance from the terrain.

3.3. Data processing

In this section, an overview of data processing is showed in Fig. 3. The collected RGB UAV-based imagery was undergone through a photogrammetric processing in order to generate a 3D geometry of the study area. The Structure-from-Motion (SfM) was used to identify common tie points in the images and reconstruct a dense point cloud (Fig. 3a.1). The resulting 3D model is then interpolated to produce an orthophoto mosaic and a digital surface model (DSM) (Fig. 3a.2 and a.3). This last one is represented as sparse point cloud (Fig. 3a.4) according to the height data from the DSM. This 3D model is used later to calculate the surface orientation of target objects.

Orthophoto mosaics are one of the basic and most important outputs generated by UAV imagery, also forming the basis of hyperspectral systems [35]. However, the complexity associated with hyperspectral imagery acquisition and processing, in particular, the difficulty to ensure the positional accuracy, is still very challenging. The several scanlines acquired by the pushbroom sensor are associated in frames (images) by stitching. The stitching process results in a final accuracy in the decimetre range. In addition, pushbroom sensors do not allow us the use of photogrammetric software to generate 3D models. Indeed, pushbroom geometry's acquisition does not include imagery overlap which prevents the 3D models generation.

Hyperspectral data processing was carried out using Headwall SpectralView software (Fig. 3b.1). Sensor raw data counts are converted into radiance by applying a calibration process deployed at the beginning of the acquisition process. The empirical line method proposed by Smith et al. [36] is used to convert at-sensor radiance into at-surface reflectance. Therefore, the radiance estimation from hyperspectral images is calculated for each pixel by applying Eq. (1).

In this work, georectified UAV-based hyperspectral mosaic was aligned with a geometric very accurate RGB mosaic using the approach developed by Jurado et al. [32] (Fig. 3b.2). This method allowed us to automatically align hyperspectral images to the RGB orthomosaic by applying a homography derived from common image features detected in both images. However, to make possible a correct alignment between the RGB orthomosaic and hyperspectral images, both resulting outcomes were resampled to 10 cm Ground Sample Distance (GSD). After the correction of the hyperspectral image distortion, new hyperspectral swaths were generated 3b.3). Thus, for each hyperspectral sample, the surface orientation could be estimated by using height data from the DSM. This geometric correction is important to calculate the normal vector of target samples in hyperspectral images and to compute light-material interactions.

$$L_o(x, \omega_o, \lambda) = k_{1,\lambda} \cdot (\frac{\Phi_r}{\Phi_i}) - k_{2,\lambda} \quad (1)$$

where $k_{1,\lambda}$ and $k_{1,\lambda}$ are the calibration coefficients of every spectral band λ, Φ_r is the radiant flux reflected by the object captured and Φ_i is the radiant flux incidence by the sun.

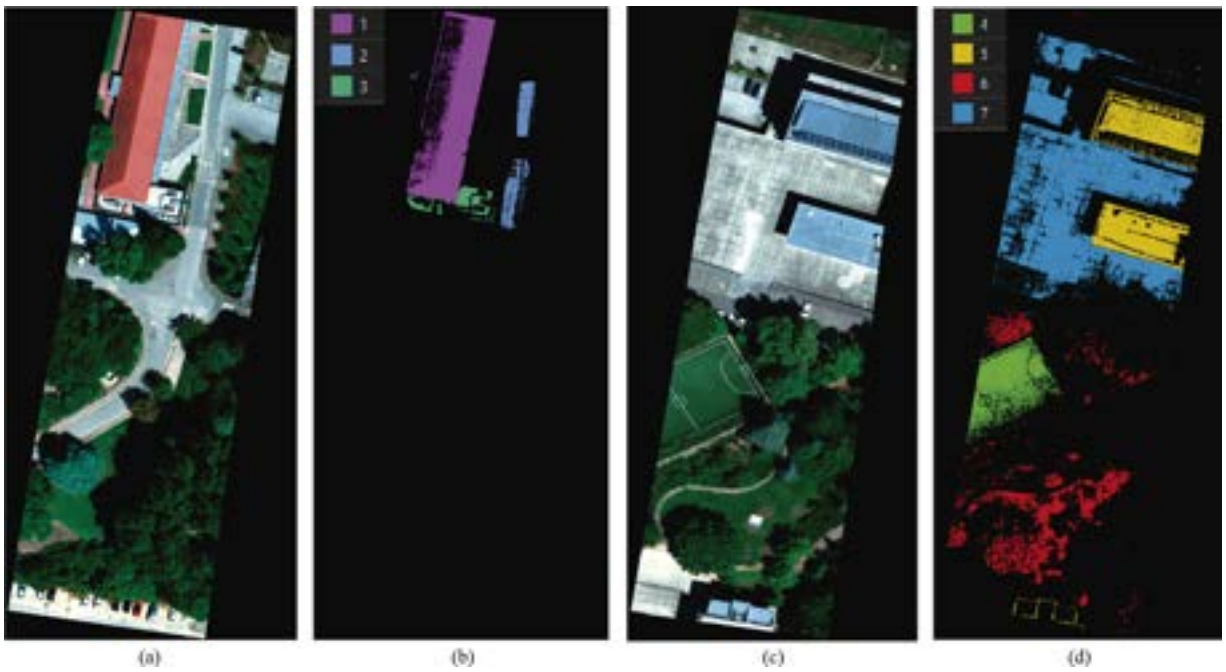

Fig. 4. Segmentation of real-world material for two hyperspectral swaths: (a) the first flight swath, (b) the mask of first three materials (roof tiles, ceramic tiles and pavement), (c) the second flight swath and (d) the mask of four more materials (artificial grass, metal roof, vegetation and granite).

Table 1
Number of samples extracted from the hyperspectral data.

ID	Description	Number of samples
1	Red roof tile	56,546
2	Ceramic tile	11,214
3	Grey pavement	5,435
4	Artificial grass	29,793
5	Metal roof	54,939
6	Vegetation	40,707
7	Granite	136,033

4. Material segmentation

The first step of our methodology is the segmentation of materials from hyperspectral images. To demonstrate the method's capabilities, seven different materials were selected which take part in captured objects such as roof tiles, artificial and natural vegetation, cars, etc. This material segmentation was performed by a semi-automatic process using the spectral angle mapper (SAM) [37]. Thus, a measure of spectral similarity was conducted in two flight swaths of the hyperspectral data. This way, given a selected spectrum of a certain material and a threshold value (between 0.1 and 0.25, depending on the material), the spectral similarity is calculated to the rest of wavelengths. This technique was used since it is relatively insensitive to illumination and albedo effects. The location of each selected material in the two flight swaths is presented in Fig. 4.

A high number of samples were selected in the hyperspectral images in order to capture from multiple viewpoints and angles the material-light interactions. Table 1 presents a summary of samples obtained for each material.

In summary, seven materials were selected, ranging from mineral-based materials (ceramic, clay and granite) to metallic materials, artificial grass and natural materials. These materials were chosen considering their variety of colour, the material composition and the hyperspectral similarity of their samples.

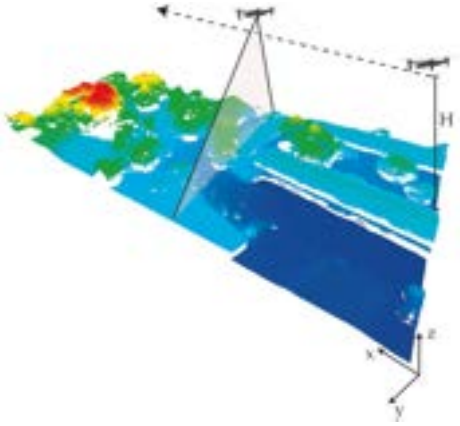

Fig. 5. The reference system used for the point cloud rendering and the calculation of all vectors for each selected material sample.

5. Characterisation of material samples

After the segmentation of target materials, every selected pixel of hyperspectral images is considered a new material sample. Each sample represents a surface's portion (10 cm x 10 cm) of real-world objects and it is characterised by three 3D vectors: (1) normal vector, (2) outgoing light vector and (3) incident light vector. Moreover, every sample provides multiple reflectance values. Regarding the capabilities of our hyperspectral sensor, 200 reflectance values with a spectral resolution of 2.2 nm are considered to measure the reflected light for each material sample. Thus, the spectrograph per sample is ranging from 440 to 900 nm.

According to the global reference system used for the calculation of the sunlight vector and the outgoing light direction, Fig. 5 shows the axes orientation where the X axis is aligned to the UAV trajectory, the Y axis is mostly related to the field of view (FoV) of the hyperspectral sensor and the Z axis is the up vector. The workflow to characterise every material sample

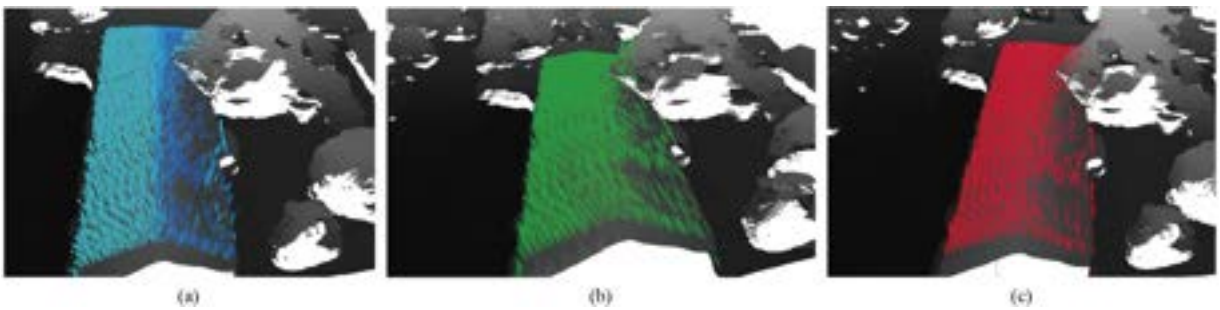

Fig. 6. A workflow for material characterisation: (a) the normal vectors, (b) the incident light vectors and (c) the outgoing light vectors.

is presented in Fig. 6. In the following sections this process is described step-by-step.

5.1. Calculation of normal vectors

The surface orientation is one of the most important features for modelling the material appearance. In this study, the estimation of normal vectors has been developed using the captured geometry by the 3D point cloud. A well-known method has been applied to estimate the local surface properties at each 3D point, in parallel, using the OpenMP standard [38]. A search of surrounding points that contribute to the normal estimation is performed by the k-nearest neighbours (kNN) algorithm. Fig. 6a shows the normal estimation for the first material that forms the roof of a building. This operation is iterated for all material samples.

5.2. Calculation of incident light vectors

According to the sunlight direction, the incident light vector is calculated by transforming the spherical coordinates of the sun position (θ, ϕ). The input data was collected from a single flight in the morning. The elevation angle was 54.62° and the azimuth angle was 137.51° considering the location of the surveyed area and the time of the flight. Eq. (2) is applied to calculate the Cartesian coordinates and thus, obtaining the components of the incident light vector (wi= X, Y, Z) for all samples. The resulting incident light vector is shown in Fig. 6b.

$$\omega_i = \{sin(\theta) \cdot cos(\phi), sin(\theta) \cdot sin(\phi), cos(\theta)\} \quad (2)$$

where ϕ is the azimuth angle, θ is the elevation angle.

5.3. Calculation of outgoing vectors

Regarding the hyperspectral sensor capture, the reflected light is observed line by line along the drone trajectory. Thus, consecutive lines compose a hyperspectral swath where every material sample is measured from a perpendicular perspective, considering the horizontal FoV of the sensor. This device enables the capture of a line formed by 640 pixels with a spatial resolution of 10 cm. Regarding parameters of the acquisition process, the outgoing vectors are calculated by applying Eq. (3)

$$\omega_o = \{0, (\frac{ccd}{2} \cdot gsd) - py \cdot gsd, h - pz\} \quad (3)$$

where *ccd* is the length of the line (640 pixels), *gsd* is the size of the pixel (0.1 m), *py* is the component Y of the sample position, *pz* is the height of the sample and *h* is the height of the drone. As a result, the direction of reflected light (ω_o) for each material sample is calculated as shown in Fig. 6c.

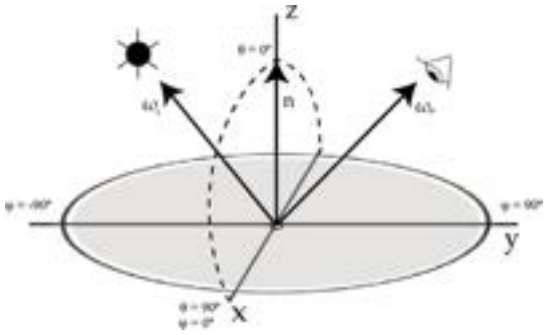

Fig. 7. The BRDF coordinate system used for sampling all measurements for each material.

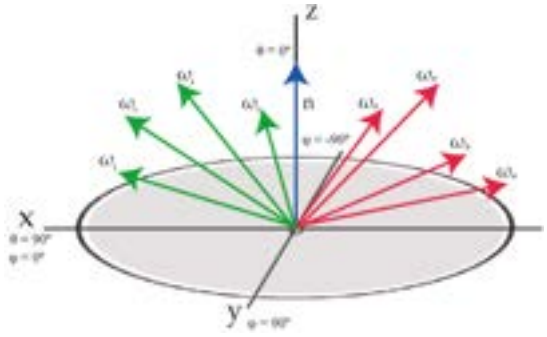

Fig. 8. A graphical representation of the BRDF space for one material after rotating incident and outgoing vectors.

5.4. Normalisation

After calculating the normal (n), the incident light (ω_i) and the outgoing (ω_o) vectors, the next step is to normalise all samples in the BRDF coordinate system as shown in Fig. 7. To this end, the normal vector of the sample has to be aligned with the normal (0,0,1). Likewise, the same 3D rotation is applied to their corresponding vectors (ω_i and ω_o) to ensure the same angle between each other.

In this study, we focus on modelling the appearance of materials considering only isotropic scattering along the material surface. Therefore, all incident light vectors (ω_i) are rotated to fix the component ϕ to 0°. The same rotation is applied to its corresponding outgoing light vector (ω_o) for each sample.

After sampling all measurements to the BRDF space, multiple ω_i and ω_o characterise every material as shown in Fig. 8. In this context, the variability of normal vectors plays an essential role to achieve a higher or lower BRDF occupation. This is discussed further in the section below.

Table 2
The overall occupation (%) of the BRDF and the coverage (%) for each incident light direction range where $\theta_1 \in [0°, 20°)$, $\theta_2 \in [20°, 40°)$, $\theta_3 \in [40°, 60°)$ and $\theta_4 \in [60°, 80°]$.

ID	Description	θ_1	θ_2	θ_3	θ_4	Coverage
1	Red roof tile	24	38	17	7	21
2	Ceramic tile	0	18	14	1.5	8
3	Grey pavement	23	38	23	4	22
4	Artificial grass	18	30	18	5	18
5	Metal roof	24	43	39	16	30
6	Vegetation	44	53	37	15	37
7	Granite	24	51	39	18	33

Table 3
The overall coverage (%) of normal vectors and the occupation (%) for each incident light direction range where $\theta_1 \in [0°, 20°)$, $\theta_2 \in [20°, 40°)$, $\theta_3 \in [40°, 60°)$ and $\theta_4 \in [60°, 80°]$.

ID	Description	θ_1	θ_2	θ_3	θ_4	Coverage
1	Red roof tile	12	27	16	5	15
2	Ceramic tile	0.7	14	6	1	5.8
3	Grey pavement	12	26	16	2	14
4	Artificial grass	10	22	14	3	12
5	Metal roof	11	25	19	8	16
6	Vegetation	12	31	23	11	19.8
7	Granite	10	28	19	7	16.3

The next step is to calculate the BRDF value per material sample. The main goal of the BRDF in a rendering context is the evaluation of the rendering formula (Eq. (4)).

$$L_o(x, \omega_o, \lambda) = \int_{\Omega} f_r(\omega_i, \omega_o, \lambda)(\omega_i \cdot n) L_i(x, \omega_i, \lambda) d\omega_i \tag{4}$$

where $L_o(x, \omega_o, \lambda)$ is the outgoing radiance captured by the camera, $f_r(\omega_i, \omega_o, \lambda)$ is the BRDF of the material, $(\omega_i \cdot n)$ is the geometrical factor determined by the angle between the normal surface and the incident light vector, $L_i(x, \omega_i, \lambda)$ is the incoming radiance from the solid angle (ω_i).

The calculation of the BRDF values is developed considering that the incident light direction is determined by the sunlight since this represents the most significant light source. Therefore, a simplified version, as shown in Eq. (5), is used in order to calculate the BRDF for each material.

$$f_{r,s}(\omega_{\text{SUN}}, \omega_o, \lambda) \simeq \frac{L_o(x, \omega_o, \lambda)}{(\omega_{\text{SUN}} \cdot n) L_i(x, \omega_{\text{SUN}}, \lambda) \Delta\omega_{\text{SUN}}} \tag{5}$$

where $L_i(x, \omega_{\text{SUN}}, \lambda)$ represents the solar radiation considering the sun position during the time flight. According to the aforementioned process, all spectral measurements of target materials are used to model their appearance and the spectral BRDF.

6. Results

In this section, we show how to leverage the theory, described before, to model spectral BRDFs using a UAV-based hyperspectral sensor. We describe our experimental setup and the spatial distribution of material samples from one drone flight.

6.1. Coverage of BRDF materials

Our method relies on an adaptive parametrisation to discretise the BRDF over incident directions. The idea is to divide the elevation between a uniform angular distribution. This has the effect of concentrating more samples and achieving a higher BRDF coverage. In this study, four different incident light direction regions were selected, changing the elevation angle from 0° to 80°. Table 2 shows the results of the BRDF space coverage.

The BRDF space coverage is significantly influenced by the variability of sample normals. The distribution of normals for each material along the hemisphere is presented in Table 3.

As mentioned, the surface orientation of material samples is key to reach a higher coverage of the BRDF space. For instance, materials such as vegetation and granite present a normal-based coverage of 19.8 and 16.3 respectively. Likewise, both materials present the highest BRDF coverage close to 40% for a single flight. Regarding the BRDF parametrisation, we define a resolution of 16 × 16 in order to spatially discretise the BRDF domain for outgoing directions of every material along the spectrum. Therefore, we assume discrete sections for range [0°, 360°] on one axis and [0°, 90°] on the other. Fig. 9 shows the heat maps that represent the hemispheric coverage considering all outgoing vectors for each incident light. A high number of samples were initially captured but many of them just represent the same area following our parametrisation. A specific pattern is appreciated for each subspace since all samples were captured during one flight where the sunlight position does not change. To complete the BRDF coverage, the proposed methodology for efficient spectral BRDF materials by consecutive flights at different times of the day (sunrise, midday and sunset) should be iterated.

Table 4
The estimation of the BRDF space occupation (%) by increasing the number of flights. This forecast is estimated by increasing one, two and four flights.

ID	Description	1	2	4
1	Red roof tile	21	35	63
2	Ceramic tile	8	9	24
3	Grey pavement	22	31	59
4	Artificial grass	18	28	54
5	Metal roof	30	35	72
6	Vegetation	37	51	86
7	Granite	33	43	79

6.2. Analysis of the BRDF samples

The variability of material samples has been analysed considering every subspace of the BRDF. Specifically, the evaluation comprises the subspaces defined by the four categories of the incident light and the 16 × 16 ones of the outgoing directions. The average and the standard deviation of all the BRDF samples in a given subspace have been calculated. We have measured the variability of a given material by the ratio between the standard deviation and the mean of the BRDF values of all regions in which it is discretised. Most material range from 0.18 to 0.22 ratio, except for the ceramic material (0.11) and vegetation (0.36).

Fig. 10 shows the BRDF values for each material, considering the four incident light directions. These results were obtained by selecting the spectral band 100 (660–662 nm) but the others can be also reviewed using Tekari software [12]. In general, most materials present the highest values on some specific cells of the BRDF space when the angle between the normal and the incoming light vector increases. Undoubtedly, more samples are required to get a full coverage of the BRDF space and thus, modelling the material appearance for each material. In this sense, a brief study is carried out to estimate how the BRDF space of each material could be completed according to further drone flights in the study area. Table 4 shows an estimation of the BRDF coverage for two and four flights at different times of the day in our study area.

According to this forecast, the increase in the BRDF space coverage is significant with additional flights at different times of the day. In particular, as mentioned before, those materials with a higher variability of normal vectors present a significant increase of the occupation. For instance, the vegetation and granite materials are covered by 86% and a 79% respectively for four flights.

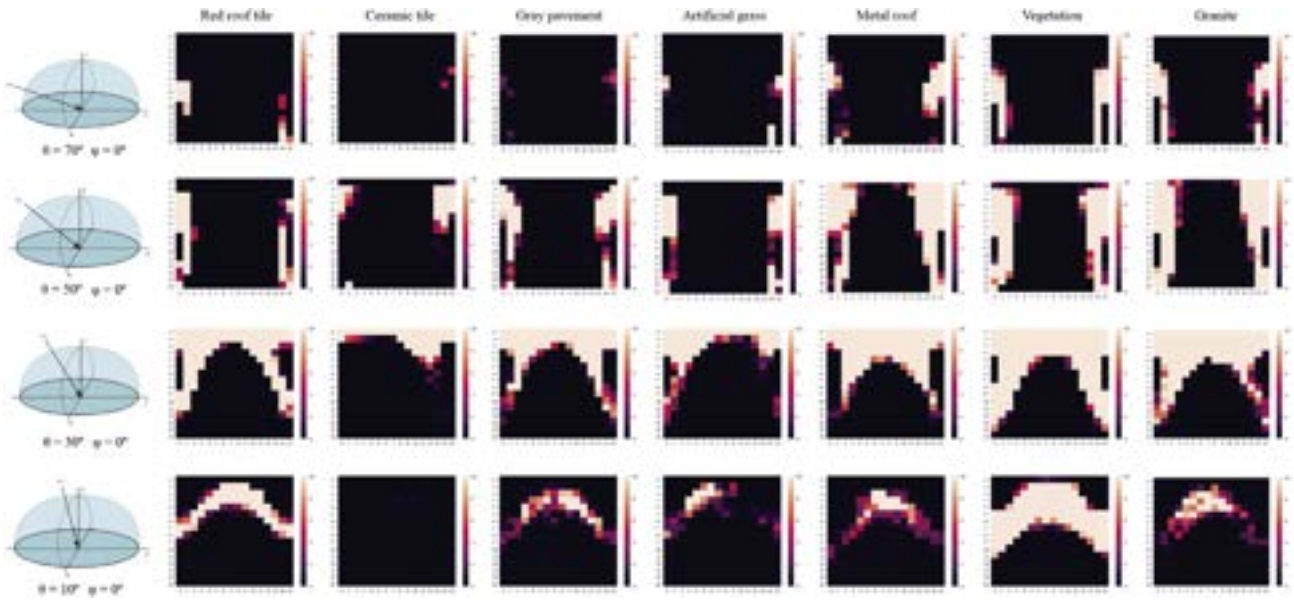

Fig. 9. Overview of the BRDF coverage for each subspace of incident light vectors. The scale of heat maps is set from 0 to 10 samples for each cell. The range of each subimage is composed this way, the (X, Y) axes represent the θ [0°, 90°] and ϕ [0°, 360°] components of the outgoing direction, respectively.

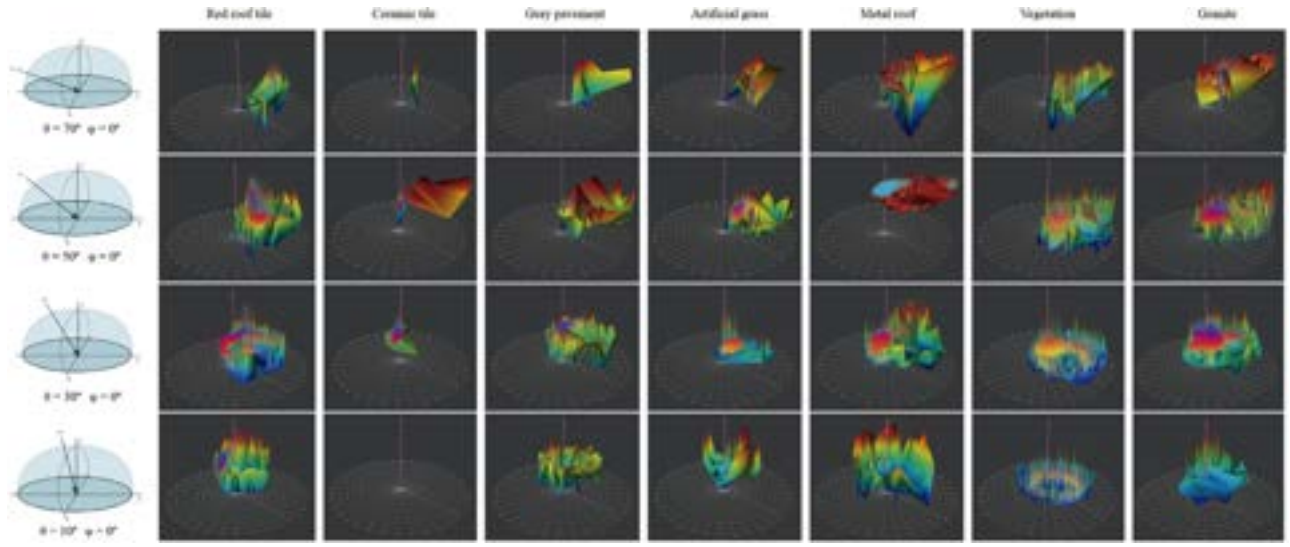

Fig. 10. Rendering of BRDF values for all samples corresponding to every subspace for each studied material.

7. Discussion

The proposed method is a disruptive solution to capture the appearance of materials of the real world beyond the visible range. One of the main concerns of this approach is the completeness of the BRDF. The results show the dependency between the normal variability and the hemisphere occupation by captured samples. An important factor to get a high BRDF coverage is the variation of outgoing and incoming directions, which increases by multiple acquisitions considering different sun inclinations. In this study, all samples were collected at the same time of day since we aim to pose the method's capabilities for a single flight. The results show that this initial limitation may be overcome by the variability of the normal vector of the samples. We observe that those materials with a higher uniform distribution of the normal vector have a lower representation. Undoubtedly, new flights can extend the number of samples as well as the completeness of the material BRDF. Additionally, regarding effectiveness of the proposed method multiple materials are captured at the same time which favours a parallel processing.

This work was focused on showing UAV-based sensors as an adequate alternative to efficiently capture spectral data and 3D geometry. In fact, these can be used for modelling the BRDF of real-world materials. The measurement of reflectance data in outdoor scenarios poses many challenges. The complex geometry of observed materials and indirect lighting cause strange reflections that could derive to unexpected errors during the material scanning process. As contribution to previous research [2,12,18], the possibility to collect measured BRDFs of materials that cannot be directly monitored in the laboratory opens novel research line by following the proposed methodology. The proposed research has inherent challenges such as BRDF coverage as previously commented, and the influence of external factors as indirect lighting and interreflections, which do not happen under laboratory constrains. In order to analyse, not only the data distribution but the value of reflectance measurements for each material, Table 5 illustrates the variability of material samples. According to the

Table 5
The maximum ratio of the variance variability for each material considering the proposed BRDF space subdivision. For these results we have discarded outliers, i.e., 10% of the samples.

ID	Description	Maximum variance (%)
1	Red roof tile	45
2	Ceramic tile	15
3	Grey pavement	33
4	Artificial grass	31
5	Metal roof	50
6	Vegetation	48
7	Granite	25

proposed subdivision of the BRDF space (16×16) for outgoing directions, materials such as the ceramic tile and granite present the lowest variance whereas vegetation, red tiles and metal roof have a higher data variability. According to our forecast varying the time of flights will increase the BRDF coverage. Regarding our current results we can observe that shiny materials and the normal estimation for irregular geometry impact the accuracy of the measurements. These shortcomings will be overcome with new flights at several times day under different illumination and with a continuous refinement of the 3D point cloud and hyperspectral dataset.

In this paper, we propose a robust pipeline to acquire measured reflectance data in outdoor scenarios and also a discrete parametrisation of the BRDF materials of the real world. Given the promising results of this method, this research means an important advance for the efficient and accurate acquisition of real-world materials characterised by high-resolution spectral measurements from surfaces of arbitrary roughness. Consequently, several applications directly benefit from our method such as (1) spectral and photorealistic rendering [39] by the use of specific spectral-BRDF materials which could be captured where they exist in real scenarios; (2) the semantic classification of real-word environments by the characterisation of the surveyed materials [40]; modelling of heterogeneous real-world materials [41,42]; and (4) the extension of material databases with new BRDF materials characterised with measured reflectance data [43,44]. Moreover, this research brings opportunities not only to the computer graphics community, by helping in rendering a wide variety of BRDF materials, but may be useful for the detection of diseases in forests [45], tree species segmentation [46], the estimation of leaf area index [47,48] and other remote sensing applications [49,50]. In this topic, most studies rely on data with coarse spatial resolutions and noise due to potential atmospheric inferences. To the best of authors' knowledge the proposed method is one of the first studies to explore UAV-based hyperspectral data for BRDF computation since previous studies are based on broadband data, by using multi-camera systems [51] or NIR imagery [52].

8. Conclusions and future work

In this research, a method for efficient acquisition of BRDF material in real-world scenarios is proposed. A UAV-based hyperspectral sensor was used to collect multiple measurements of seven different materials (red roof tile, ceramic tile, grey pavement, artificial grass, metal roof, vegetation and granite). According to the application of the proposed method, these materials are formed by many samples that are characterised by the outgoing light direction, the reflected radiance, 200 values with a spectral resolution of 2.2 nm, the incident light vector and the normal vector.

Our method is based on an adaptive parametrisation to discretise the BRDF over incident directions. The results demonstrated the capabilities of our method and hyperspectral technology to efficiently collect accurate spectral reflectance of real-world materials and sampling every hyperspectral measurement on the BRDF space. Likewise, in this study, the coverage of the BRDF is analysed for one flight as well as a coarse estimation to achieve a higher occupation by more flights. In addition, the BRDF variability for each material is partially obtained, considering the input dataset.

As further research, we will focus on the production of our own material database and BRDF parametrisation for modelling the material appearance using this method to acquire multiple samples of captured materials in real-world scenarios. In addition, we will explore validation methods by comparing our measurements with others acquired in the laboratory and algorithms to provide a fully automatic segmentation of materials from hyperspectral data.

CRediT authorship contribution statement

Juan M. Jurado: Ideas, Development or design of methodology, Programming, Specifically performing the experiments, or data/evidence collection, Writing – review & editing. **J. Roberto Jiménez-Pérez:** Development or design of methodology, Programming, Specifically performing the experiments, or data/evidence collection, Writing – review & editing, Testing of existing code components, Computing resources, Supervision. **Luís Pádua:** Ideas, Writing – review & editing, Supervision. **Francisco R. Feito:** Ideas, Writing – review & editing, Supervision. **Joaquim J. Sousa:** Ideas, Provision of study materials, Writing – review & editing, Supervision.

Declaration of competing interest

The authors declare that they have no known competing financial interests or personal relationships that could have appeared to influence the work reported in this paper.

Acknowledgement

This research was partially funded by the Ministry of Science and Innovation of Spain and the European Union (via ERDF funds), through the research project TIN2017-84968-R.

References

[1] Kurt M, Edwards D. A survey of brdf models for computer graphics. ACM SIGGRAPH Comput Grap 2009;43(2):1–7.
[2] Matusik W, Pfister H, McMillan L, Brand M. MIT/Merl BRDF Database. BRDF; 2003, http://graphics.csail.mit.edu/~wojciech.
[3] Filip J, Vávra R. Template-based sampling of anisotropic brdfs. In: Comput Graph Forum. 33, (7):Wiley Online Library; 2014, p. 91–9.
[4] Xu Z, Nielsen JB, Yu J, Jensen HW, Ramamoorthi R. Minimal brdf sampling for two-shot near-field reflectance acquisition. ACM Trans Graph 2016;35(6):1–12.
[5] Holzschuch N, Pacanowski R. A two-scale microfacet reflectance model combining reflection and diffraction. ACM Trans Graph 2017;36(4):1–12.
[6] Serrano A, Gutierrez D, Myszkowski K, Seidel H-P, Masia B. An intuitive control space for material appearance. ACM Trans Graph 2016;35(6). http://dx.doi.org/10.1145/2980179.2980242.
[7] Lagunas M, Malpica S, Serrano A, Garces E, Gutierrez D, Masia B. A similarity measure for material appearance. ACM Trans Graph (SIGGRAPH 2019) 2019;38(4).
[8] Vilaseca M, Schael B, Delpueyo X, Chorro E, Perales E, Hirvonen T, Pujol J. Repeatability, reproducibility, and accuracy of a novel pushbroom hyperspectral system. Color Res Appl 2014;39(6):549–58. http://dx.doi.org/10.1002/col.21851.
[9] Xiong F, Zhou J, Qian Y. Material based object tracking in hyperspectral videos. IEEE Trans Image Process 2020;29:3719–33.
[10] Dawson P, Shettigara V. Improving detection using a material pattern matching technique in hyperspectral images. In: 2013 IEEE international geoscience and remote sensing symposium - IGARSS; 2013. p. 425–8.

[11] Sundberg R, Adler-Golden S, Perkins T, Vongsy K. Detection of spectrally varying BRDF materials in hyperspectral reflectance imagery. In: 2015 7th workshop on hyperspectral image and signal processing: evolution in remote sensing (WHISPERS); 2015. p. 1–4.
[12] Dupuy J, Jakob W. An adaptive parameterization for efficient material acquisition and rendering. Trans Graph (Proceedings of SIGGRAPH Asia) 2018;37(6):274:1–274:18. http://dx.doi.org/10.1145/3272127.3275059.
[13] Park K, Rematas K, Farhadi A, Seitz SM. Photoshape: Photorealistic materials for large-scale shape collections. ACM Trans Graph 2018;37(6). http://dx.doi.org/10.1145/3272127.3275066.
[14] Stomakhin A, Schroeder C, Chai L, Teran J, Selle A. A material point method for snow simulation. ACM Trans Graph 2013;32(4). http://dx.doi.org/10.1145/2461912.2461948.
[15] Guarnera D, Guarnera GC, Ghosh A, Denk C, Glencross M. Brdf representation and acquisition. In: Computer graphics forum. 35, (2):Wiley Online Library; 2016, p. 625–50.
[16] Apian-Bennewitz P. New scanning gonio-photometer for extended brtf measurements. In: Reflection, scattering, and diffraction from surfaces II. 7792, International Society for Optics and Photonics; 2010, p. 77920O.
[17] Dana KJ. Brdf/btf measurement device. In: Proceedings eighth ieee international conference on computer vision. ICCV 2001. 2, IEEE; 2001, p. 460–6.
[18] Vávra R, Filip J. Minimal sampling for effective acquisition of anisotropic brdfs. In: Computer graphics forum. 35, (7):Wiley Online Library; 2016, p. 299–309.
[19] Yang SK, Song I-U, Oh E, Yang H-S, Kim S-W. Development of a new image based brdf measurement system using a semicircular ring. In: Reflection, scattering, and diffraction from surfaces VII. 11485, International Society for Optics and Photonics; 2020, p. 114850M.
[20] Jarabo A, Wu H, Dorsey J, Rushmeier H, Gutierrez D. Effects of approximate filtering on the appearance of bidirectional texture functions. IEEE Trans Vis Comput Graphics 2014;20(6):880–92.
[21] Sun T, Jensen HW, Ramamoorthi R. Connecting measured brdfs to analytic brdfs by data-driven diffuse-specular separation. ACM Trans Graph 2018;37(6). http://dx.doi.org/10.1145/3272127.3275026.
[22] Zsolnai-Fehér K, Wonka P, Wimmer M. Gaussian material synthesis. ACM Trans Graph 2018;37(4). http://dx.doi.org/10.1145/3197517.3201307.
[23] Hu B, Guo J, Chen Y, Li M, Guo Y. Deepbrdf: A deep representation for manipulating measured brdf. Comput Graph Forum 2020;39(2):157–66. http://dx.doi.org/10.1111/cgf.13920.
[24] Baek S-H, Zeltner T, Ku HJ, Hwang I, Tong X, Jakob W, Kim MH. Image-based acquisition and modeling of polarimetric reflectance. ACM Trans Graph 2020;39(4). http://dx.doi.org/10.1145/3386569.3392387.
[25] Muller T, Callet P, Paljic A, Porral P. Predictive rendering of composite materials, a multi-scale approach. In: Measuring, modeling, and reproducing material appearance 2015. San Francisco, United States; 2015, http://dx.doi.org/10.1117/12.2077920.
[26] Adão T, Hruška J, Pádua L, Bessa J, Peres E, Morais R, Sousa J. Hyperspectral imaging: A review on uav-based sensors, data processing and applications for agriculture and forestry. Remote Sens 2017;9(11):1110. http://dx.doi.org/10.3390/rs9111110.
[27] Sowmya V, Soman K, Hassaballah M. Hyperspectral image: Fundamentals and advances. In: Hassaballah M, Hosny KM, editors. Recent advances in computer vision: Theories and applications. Cham: Springer International Publishing; 2019, p. 401–24. http://dx.doi.org/10.1007/978-3-030-03000-1_16.
[28] Mahesh S, Jayas D, Paliwal J, White N. Hyperspectral imaging to classify and monitor quality of agricultural materials. J Stored Products Res 2015;61:17–26.
[29] Martin JA, Gross KC. Enhanced material identification using polarimetric hyperspectral imaging. In: 2014 IEEE applied imagery pattern recognition workshop (AIPR). Los Alamitos, CA, USA: IEEE Computer Society; 2014, p. 1–6. http://dx.doi.org/10.1109/AIPR.2014.7041920.
[30] Chen B, Shi S, Sun J, Gong W, Yang J, Du L, Guo K, Wang B, Chen B. Hyperspectral lidar point cloud segmentation based on geometric and spectral information. Opt Express 2019;27(17):24043–59.
[31] Brell M, Segl K, Guanter L, Bookhagen B. 3D hyperspectral point cloud generation: Fusing airborne laser scanning and hyperspectral imaging sensors for improved object-based information extraction. ISPRS J Photogramm Remote Sens 2019;149:200–14.
[32] Jurado JM, Padua L, Hruska J, Feito FR, Sousa JJ. An efficient method for generating UAV-based hyperspectral mosaics using push-broom sensors. IEEE J Sel Top Appl Earth Obs Remote Sens 2021. http://dx.doi.org/10.1109/JSTARS.2021.3088945, 1–1.
[33] Lombardi S, Nishino K. Reflectance and natural illumination from a single image. In: European conference on computer vision. Springer; 2012, p. 582–95.
[34] Pádua L, Sousa J, Vanko J, Hruška J, Adão T, Peres E, Sousa A, Sousa JJ. Digital reconstitution of road traffic accidents: A flexible methodology relying on UAV surveying and complementary strategies to support multiple scenarios. Int J Environ Res Public Health 2020;17(6):1868. http://dx.doi.org/10.3390/ijerph17061868.
[35] Zarco-Tejada P, Diaz-Varela R, Angileri V, Loudjani P. Tree height quantification using very high resolution imagery acquired from an unmanned aerial vehicle (UAV) and automatic 3D photo-reconstruction methods. Eur J Agron 2014;55:89–99. http://dx.doi.org/10.1016/j.eja.2014.01.004.
[36] Smith GM, Milton EJ. The use of the empirical line method to calibrate remotely sensed data to reflectance. Int J Remote Sens 1999;20(13):2653–62. http://dx.doi.org/10.1080/014311699211994.
[37] Kruse F, Lefkoff A, Boardman J, Heidebrecht K, Shapiro A, Barloon P, Goetz A. The spectral image processing system (SIPS)—interactive visualization and analysis of imaging spectrometer data. Remote Sens Environ 1993;44(2):145–63. http://dx.doi.org/10.1016/0034-4257(93)90013-N, Airbone Imaging Spectrometry.
[38] Boulch A, Marlet R. Fast and robust normal estimation for point clouds with sharp features. In: Computer graphics forum. 31, (5):Wiley Online Library; 2012, p. 1765–74.
[39] Peters C, Merzbach S, Hanika J, Dachsbacher C. Using moments to represent bounded signals for spectral rendering. ACM Trans Graph 2019;38(4). http://dx.doi.org/10.1145/3306346.3322964.
[40] Yi L, Gong B, Funkhouser T. Complete & label: A domain adaptation approach to semantic segmentation of LiDAR point clouds. In: Proceedings of the IEEE/CVF conference on computer vision and pattern recognition; 2021. p. 15363–73.
[41] F. C-R, Á-.L. G-F, J.C. T. Modelling material microstructure using the perlin noise function. Comput Graph Forum 2021;40(1):195–208. http://dx.doi.org/10.1111/cgf.14182.
[42] F. C-R, Á-.L. G-F, J.C. T. Modeling the internal architecture of composites. Comput Aided Des 2020;129:102930. http://dx.doi.org/10.1016/j.cad.2020.102930.
[43] Igouchkine O, Zhang Y, Ma K. Multi-material volume rendering with a physically-based surface reflection model. IEEE Trans Vis Comput Graphics 2018;24(12):3147–59. http://dx.doi.org/10.1109/TVCG.2017.2784830.
[44] Guo J, Guo Y, Pan J, Lu W. Brdf analysis with directional statistics and its applications. IEEE Trans Vis Comput Graphics 2020;26(3):1476–89. http://dx.doi.org/10.1109/TVCG.2018.2872709.
[45] Degerickx J, Roberts D, McFadden J, Hermy M, Somers B. Urban tree health assessment using airborne hyperspectral and lidar imagery. Int J Appl Earth Obs Geoinf 2018;73:26–38. http://dx.doi.org/10.1016/j.jag.2018.05.021.
[46] Zhang B, Zhao L, Zhang X. Three-dimensional convolutional neural network model for tree species classification using airborne hyperspectral images. Remote Sens Environ 2020;247:111938. http://dx.doi.org/10.1016/j.rse.2020.111938.
[47] Hasegawa K, Matsuyama H, Tsuzuki H, Sweda T. Improving the estimation of leaf area index by using remotely sensed ndvi with brdf signatures. Remote Sens Environ 2010;114(3):514–9.
[48] Qi J, Kerr Y, Moran M, Weltz M, Huete A, Sorooshian S, Bryant R. Leaf area index estimates using remotely sensed data and brdf models in a semiarid region. Remote Sens Environ 2000;73(1):18–30.
[49] Gatebe CK, King MD. Airborne spectral brdf of various surface types (ocean, vegetation, snow, desert, wetlands, cloud decks, smoke layers) for remote sensing applications. Remote Sens Environ 2016;179:131–48.
[50] Lucht W, Roujean J-L. Considerations in the parametric modeling of brdf and albedo from multiangular satellite sensor observations. Remote Sens Rev 2000;18(2–4):343–79.
[51] Grenzdörffer G, Niemeyer F. Uav based brdf-measurements of agricultural surfaces with pfiffikus. Int Arch Photogramm Remote Sens Spat Inf Sci 2011;38(1/C22):229–34.
[52] Wierzbicki D, Kedzierski M, Fryskowska A, Jasinski J. Quality assessment of the bidirectional reflectance distribution function for nir imagery sequences from uav. Remote Sens 2018;10(9):1348.